PHYSICAL REVIEW B **88**, 035306 (2013)

Influence of facets on solid state dewetting mechanisms: Comparison between Ge and Si on SiO_2

F. Leroy,[*] F. Cheynis,[†] T. Passanante, and P. Müller[‡]
CINaM, UMR CNRS 7325, Campus de Luminy, Aix-Marseille University, 13288 Marseille Cedex, France
(Received 7 May 2013; published 15 July 2013)

The dewetting properties of Ge/SiO_2 have been studied by low-energy electron microscopy and grazing incidence small-angle x-ray scattering in two temperature ranges characterized by the presence or the absence of {15 3 23} facets on the dewetting fronts. Thanks to a comparison with the Si/SiO_2 system, we show that the {15 3 23} facets: (i) play a role in the stabilization properties of Ge dewetting fronts, (ii) lead to a rotation of 45° of the Ge fingers with respect to the Si fingers, and (iii) increase the Ge fingers' stability delaying the formation of a three-dimensional Ge islands with respect to Si for the benefit of the formation of Ge nanowires. Studying the dewetting kinetics enables estimating the activation energy for Ge dewetting to 2.7 ± 0.2 eV. The weak energetics differences between Si and Ge systems are sufficient to change the dewetting morphologies from a squared-void opening for Si/SiO_2 to multibranch dendrites for Ge with specific consequences on the relative dewetting velocities of the Si/SiO_2 and Ge/SiO_2 systems.

DOI: 10.1103/PhysRevB.88.035306 PACS number(s): 68.35.Md, 68.37.−d, 68.60.Dv, 68.55.J−

I. INTRODUCTION

Solid state dewetting of thin films is a process by which a metastable film uncovers its substrate and agglomerates into an assembly of three-dimensional (3D) islands. Solid state dewetting is, thus, a common 2D → 3D transformation (where 2D represents two-dimensional). Continuous models based on surface diffusion[1–3] predict that, during dewetting, the film material removed from the substrate accumulates into a rim followed by a depression. During dewetting, the rim thickens, and the depression deepens so that, when the depression reaches the substrate, the film breaks and leaves a crystalline one-dimensional (1D) island in front of a new dewetting front. This repeated pinch-off mechanism is at the origin of a periodic mass shedding process.[4,5] However, continuous models based on the standard concept of curvature-driven surface diffusion cannot be directly applied to anisotropic materials. In particular, for anisotropic materials, the stability conditions of a dewetting front as well as its receding velocity are governed by the presence or the absence of atomically flat facets along the receding front edge as illustrated by experimental studies of dewetting fronts[6] or anisotropic edge retraction velocities.[7] More precisely, the concept of curvature-driven surface diffusion must be replaced by a new description[3,6,8] in which enter: (i) the driving force for dewetting expressed in terms of the local thickness of the dewetting front[5,9] and (ii) the local morphology of the receding front.[6] The importance of this latter ingredient has been particularly well illustrated in the case of Si(001) thin films on an amorphous SiO_2 substrate [$Si(001)/aSiO_2$].[6,10,11] Indeed, for $Si(001)/aSiO_2$, ⟨110⟩-oriented dewetting fronts are stabilized by {111} and {113} facets and, thus, recede keeping their initial straight shapes, whereas, ⟨100⟩-oriented fronts are destabilized and, thus, recede by forming periodic Si fingers separated by void fingers.[6,11] It results in a strong kinetics anisotropy since the ⟨100⟩ front velocity is about 10 times the ⟨110⟩ front velocity.[6]

This paper specially concerns the effects of facets on the dewetting properties of an anisotropic material. Our goal was to select a material for which stability conditions and the anisotropy retraction of a dewetting front can be controlled by tuning the facet formation. For this purpose, we have selected the $Ge(001)/aSiO_2$ system. Indeed, we will show that Ge exhibits {15 3 23} facets that can be "switched off" or can be "switched on" by varying the temperature.

The paper is set in five parts. In Sec. II, we describe the experiments. Section III is devoted to a study of the crystallographic facet characteristics of the Ge dewetted state. A coupled low-energy electron microscopy- (LEEM-) atomic force microscopy (AFM) study of the dewetting morphology as well as a study of the dewetting kinetics are reported in Sec. IV. Since $Si(001)/aSiO_2$ and $Ge(001)/aSiO_2$ systems can be considered as "brother systems" (they have five common stable facets and similar energetics since Ge bonds are simply around 20% weaker than Si bonds[12]), Sec. V is devoted to a comparison between $Ge(001)/aSiO_2$ and $Si(001)/aSiO_2$ systems. Finally, conclusions are given in Sec. VI.

II. EXPERIMENT

The dewetting experiments have been performed with low-energy electron microscope-photoemission electron microscope (LEEM-PEEM) (Elmitec LEEM-PEEM III) at high temperatures (typically, 800 °C) under pressures below 10^{-9} Torr. The samples are bonded germanium on insulator (GOI) and silicon on insulator (SOI) obtained from CEA-Leti, France.[13,14] They are composed of stress-free single-crystal Si(001) films (22 ± 2-nm thick) or Ge(001) (55 ± 2-nm thick) on an ∼150-nm-thick amorphous SiO_2 film. The SOI samples are cleaned by using a published recipe,[15] whereas, GOI samples are prepared by *in situ* outgassing at 600 °C for several hours (typically, 12 h) followed by 1-h cycles of Ar^+-ion sputtering at normal incidence at room temperature under a partial pressure of $P \sim 5.10^{-6}$ Torr and a bombardment voltage of $V = 1$ keV ($I_{sample} \sim 6\ \mu$A). After ion bombardment, the sample is annealed at 500–600 °C to heal the defects induced by the ion bombardment. The thickness reduction during the ion bombardment allows us to obtain several film thicknesses varying between 18 and 32 nm. The final Ge thickness has been measured *ex situ* by atomic force microscopy after partial dewetting of the film and by independent x-ray diffraction

 ©2013 American Physical Society

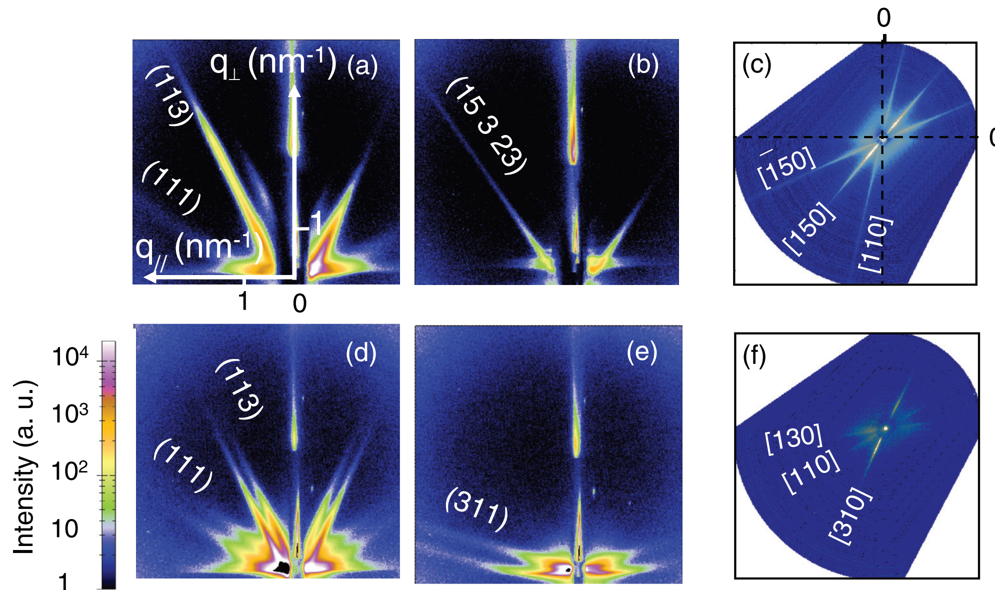

FIG. 1. (Color online) GISAXS measurements of the GOI film at $T = 800\,^{\circ}$C (on top) and $T = 890\,^{\circ}$C (bottom). Extended scattering rods from (113) and (111) facets are observed at (a) $T = 800\,^{\circ}$C and at (d) $T = 890\,^{\circ}$C when the incident beam is aligned in the $\langle 1\bar{1}0\rangle$ direction. Rotating the sample by 34°, (15 3 23) facets are observed at (b) $T = 800\,^{\circ}$C, whereas, (311) facets are observed at (e) $T = 890\,^{\circ}$C. Planar projections of the GISAXS intensities are reported in (c) and (f).

measurements.[16] Most of the dewetting experiments have been recorded *in situ* by PEEM or by LEEM. PEEM and LEEM image sequences are recorded at a fixed rate (0.3–1 Hz) to form a movie of the dewetting process. In LEEM, we have used bright-field, dark-field, and tilted bright-field imaging modes in which images are formed either from a reflected spot, 1/2-order diffraction beam associated with the $X(100)$-2×1 and $X(100)$-1×2 ($X =$ Ge,Si) surface reconstructions or from a tilted incident beam. As adjacent terraces have orthogonal surface reconstructions, dark-field and tilted bright-field modes give rise to a bright/dark contrast that reveals the steps' organization at the surface. The LEEM measurements simultaneously show the micrometer-scale structure of the dewetting front, the nanoscale motion of surface atomic steps, and 2D nucleation events.

The facets involved in the dewetting process have been studied by *in situ* grazing incidence small-angle x-ray scattering (GISAXS) performed at the European Synchrotron Radiation Facility (ESRF BM 32 beamline, Grenoble, France). For this purpose, we have used an x-ray wavelength of 0.1169 nm and an incident angle close to the critical angle for the total external reflection of Ge ($\alpha_c = 0.23°$). The GISAXS technique and experimental considerations as the description of the 2D detector (X-ray Image Star 9000, Photonic Science) and of the slits used to avoid background scattering are described in Ref. 17.

III. GE FACETS VERSUS TEMPERATURE: A GISAXS STUDY

The GISAXS intensities scattered by the dewetting film are measured over the reciprocal space. GISAXS patterns have been recorded at different azimuths by rotating the sample by steps of 1° over a large angular range (>90°). The GISAXS patterns show diffuse scattering rods arising from the facets of the dewetting front and the facets of the agglomerated islands. All (hkl) facets observed in GISAXS at $T = 800\,^{\circ}$C and $T = 890\,^{\circ}$C (Fig. 1) are reported in Table I. For the sake of simplicity, in the following text, we will regroup the facets by family using an *ad hoc* $\{hkl\}$ notation as reported in the first line of Table I. (For instance, the {113} notation is, thus, not equivalent to the {311} notation).

Figures 1(c) and 1(f) show planar projections of the recorded GISAXS intensities. At $T = 800\,^{\circ}$C [Fig. 1(c)], the $[\bar{1}50]$ and [150] directions that are the projections of the $(\bar{3}\,15\,23)$ and (3 15 23) facets, respectively, as well as the [110] direction that corresponds to the projection of (113) and (111) facets are observed. At $T = 890\,^{\circ}$C, Fig. 1(f) shows the [130] and [310] directions that are the projections of the (131) and (311) facets, respectively, as well as the [110] direction that is the projection of the (113) and (111) facets. The sharp in-plane scattering observed in the GISAXS projection is due to the similar orientation of all the dewetting zones as we will discuss later on in Sec. IV A.

These results confirm the high stability of {113}, {111}, and {15 3 23} facets reported by Gai and co-workers,[18–20] who have shown that Ge material has six major stable surfaces. Five of them, the (113), (001), (101), (313), and (111) stable surfaces are common to Ge and Si materials. The {15 3 23}, specific to Ge, also is a stable orientation since (i) it cannot be resolved into nanofacets of any other orientation and (ii) annealing vicinals of {15 3 23} surfaces leads to {15 3 23} microfacets.[18–20] These results are also in agreement with scarce available data on the equilibrium shape of Ge. Indeed, Ross *et al.*,[21] studying Ge islands deposited on Si(001) substrates around $T = 700\,^{\circ}$C, found that the Ge equilibrium shape is formed by {113} and {15 3 23} facets smoothly connected by rounded parts. As reported by Stekolnikov and

TABLE I. Facets observed in GISAXS.

Family	{15 3 23}	{111}	{113}	{311}
	$(15\,3\,23)(15\,\bar{3}\,23)(3\,15\,23)(\bar{3}\,15\,23)$ $(\overline{15}\,\bar{3}\,23)(\overline{15}\,3\,23)(\bar{3}\,\overline{15}\,23)(3\,\overline{15}\,23)$	$(111)(\bar{1}11)$ $(1\bar{1}1)(\bar{1}\bar{1}1)$	$(113)(\bar{1}13)$ $(1\bar{1}3)(\bar{1}\bar{1}3)$	$(311)(\bar{3}11)(131)(\bar{1}31)$ $(3\bar{1}1)(\bar{3}\bar{1}1)(1\bar{3}1)(\bar{1}\bar{3}1)$
Observed at 800 °C	*Yes*	*Yes*	*Yes*	*No*
Observed at 890 °C	*No*	*Yes*	*Yes*	*Yes*

Bechstedt,[22] the {15 3 23} surface could actually be stabilized by surface strain.

Since {15 3 23} facets do not exist at $T = 890\,^{\circ}$C (see Fig. 1) but exist at $T = 800\,^{\circ}$C, we can infer that the roughening transition of the {15 3 23} facet occurs around $T_R \approx 850\,^{\circ}$C. This temperature is close to the Ge(001) roughening temperature [≈860 °C (Ref. 23)]. Increasing the temperature close to equilibrium conditions at $T > T_R$, thus, makes the {15 3 23} facets disappear on the Ge equilibrium shape at the expense of a rounded part.

IV. DEWETTING MORPHOLOGY AND KINETICS: A COUPLED LEEM-PEEM/AFM STUDY

A. Dewetting morphologies

In the low-temperature regime ($T < T_R$), the dewetting of Ge(001)/aSiO$_2$ is initiated by the heterogeneous nucleation of voids (Figs. 2 and 3). The voids grow spontaneously with a large anisotropy of velocity. They, thus, form crosslike shapes with four void branches aligned along the ⟨110⟩ directions (Fig. 2). As shown by AFM, the voids are surrounded by a rim, characterized by a nonconstant height [Fig. 2(d)]. More precisely, the rim height varies along a branch with a decreasing amplitude away from the center of the void. In the dark-field LEEM image, recorded from a 1/2 diffracted spot, the rim summits appear dark or bright [Figs. 2(a) and 2(b)]. It means that the rim is locally faceted with a top (001) facet. Furthermore, in LEEM movies, the top facets alternatively blink from bright to dark during the dewetting, proving that the upper parts of the rim grow in a layer-by-layer mode. It is, thus, possible to measure the local rim thickening by counting the number of additive layers [Fig. 2(c)]. For initial stages, we find a linear $h(x,t) \propto t$ behavior. For completeness, notice that the flash events can only be formally observed at $T \sim 700\,^{\circ}$C (see Fig. 2) since increasing the Ge temperature promotes a reversible surface disorder with the progressive disappearance of the (1 × 2) and (2 × 1) surface reconstructions of the Ge(001) top facet.[24]

For longer times, the void branches invariably turn out to be unstable, leading to perpendicular secondary branches and then to a dendritic shape evolution (Fig. 3). Since the lower the local thickness h, the greater the local velocity,[6,9] these second branches born and develop from the thinnest parts of the rim. Thus, as predicted by Kan and Wong,[25] the lateral instability is driven by the height instability of the rim. Obviously, for kinetics reasons, the less developed secondary branches, since "younger," are close to the principal void tip. However, we

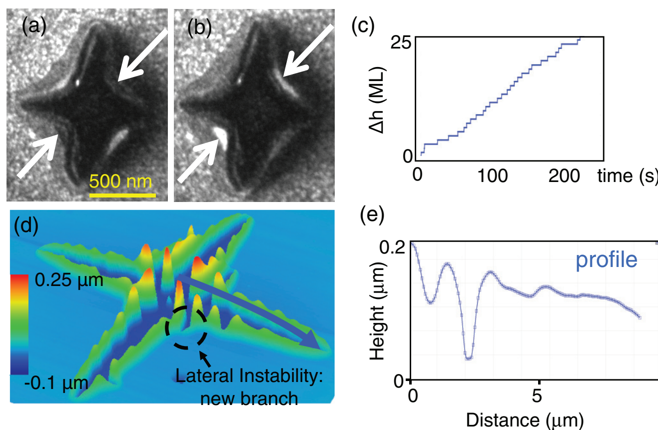

FIG. 2. (Color online) Low-temperature regime ($T \sim 700\,^{\circ}$C): (a) and (b) dark-field LEEM images recorded at t and $t + 10$ s illustrating the cross shape of the opening hole and the contrast inversion of the summit of the rim (see white arrows). From this, one can record the (c) local rim thickening expressed in monolayers (MLs) versus time. In the LEEM image, the bottom of the opening hole (the SiO$_2$ surface) is dark, the Ge surface is speckled due to the coexistence of 1 × 2 and 2 × 1 domains (area ∼100 nm^2). The rim is "shadowed" due to its 3D structure. (d) AFM 3D view of an opening void (at a longer time) illustrating (e) the height variation in the rim along a void branch.

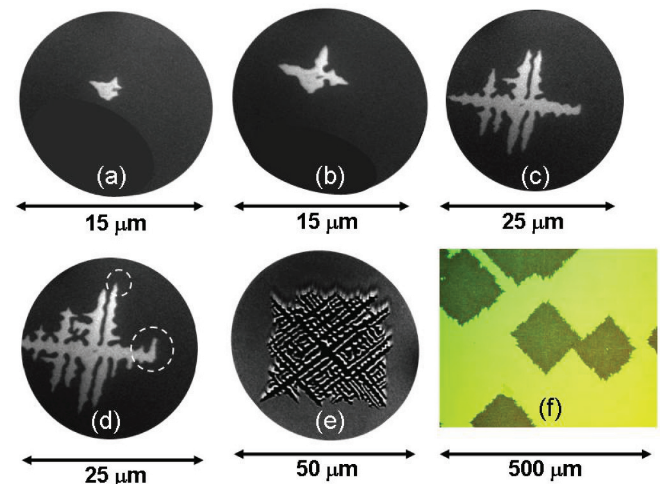

FIG. 3. (Color online) PEEM images of GeOI dewetting (40 ± 2-nm thick, $T = 800\,^{\circ}$C). The images have been taken at (a) $t = t_0$: opening void on a defect; (b) $t_0 + 1$ mn: cross-shaped formation; (c) $t_0 + 3.5$ mn: void branches with the appearance of secondary branches; (d) $t_0 + 5$ mn: branches development; (e) $t_0 + 15$ mn: square envelope limited by ⟨100⟩ edges. (f) is an optical large-scale image of dewetting that reveals several similar square-shaped dewetting areas.

cannot exclude an additional dependence of the exponential amplification coefficient of the Kan and Wong instability on the local in-plane curvature of the dewetting front as for parabolic crystals, formed by diffusion-limited growth.[26,27] Notice that the in-cascade formation of additional void branches develops a negative dendritic shape inside a square envelope limited by ⟨100⟩ edges [Fig. 3(e)]. In a few cases, a void tip encounters a defect that prevents its propagation. In this case, the void tip deviates forming a secondary orthogonal branch at its extremity [large circle in Fig. 3(d)]. The void tips are rounded and do not exhibit precise facets contrary to Si(001)/aSiO$_2$ where the void tips have been found to decompose into two microfronts oriented along the {110} directions.[6]

Finally, a large-scale optical image, that reveals several dewetting zones that have grown from different nucleation sites, is reported in Fig. 3(f). All the square-shaped zones have their sides parallel to the Ge⟨100⟩ directions. Since the nucleation events are uncorrelated,[16] this alignment of the dewetting zones is simply due to the perfect single crystallinity of the Ge(001) film, which thus, predefines the orientation of the growing dendrites. Notice that the orientation of the film is preserved during the whole dewetting process giving rise to single-crystalline nanowires and nanoislands. This common orientation is also illustrated in the sharp in-plane scattering reported in GISAXS experiments (see Fig. 1).

In the high-temperature regime ($T > T_R$), the dewetting mechanism and the dewetted morphology are similar to the low-temperature case. However, the branch density increases with the sample temperature. This is in fair agreement with classical predictions on the influence of the driving force $\Delta\mu/k_BT$ on the large-scale morphology of dendritic structures.[28]

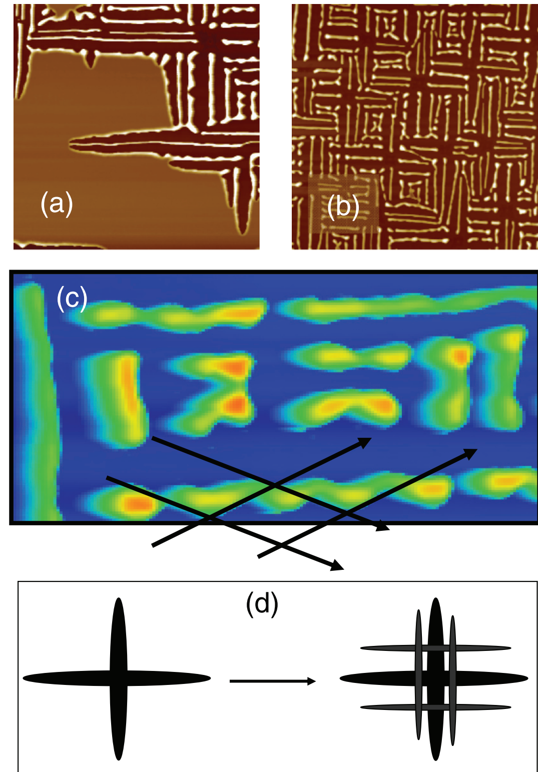

FIG. 4. (Color online) Nanowire formation. (a) AFM images of the nanowire formation (30 × 30 μm^2, the Ge material appears in white), (b) AFM image (50 × 50 μm^2) of the dewetted state exhibiting a collection of nanowires, (c) details of the nanowire's structure (10 × 6 μm^2), and (d) sketch of the nanowire formation by the crossing of principal and secondary void branches (dark).

B. Three-dimensional island formation

During dewetting, the Ge expelled from the growing void branches forms elongated structures in the ⟨110⟩ direction (see Fig. 4). The perpendicular void branches, formed by the lateral instabilities of the previous branches, intersect these elongated structures and leave Ge nanowires as seen in Figs. 4(a) and 4(b) and sketched in Fig. 4(d). These nanowires do not remain straight, but their edges mainly start to facet locally in the ⟨310⟩ and/or ⟨510⟩ directions [see Fig. 4(c)]. These directions can be associated with the presence of {311} and {15 3 23} facets and are at the origin of nanowires breaking into 3D nanoislands according to a Rayleigh-Plateau-type transition. We have noticed that the number of ⟨310⟩-oriented edges increases as a function of temperature with respect to the ⟨510⟩-oriented edges. We associate this change with the disappearance of the {15 3 23} facets due to the roughening transition.

It is observed (Fig. 4) that the number of nanowires increases with the density of side branches, whereas, a higher branch density implies shorter nanowires. It can be easily understood since the initial nanowire size (width and length) is nothing else than the interbranch distance [Fig. 4(d)]. In other words, for low branch density, nanowires are formed and give birth to 3D islands by a Rayleigh-Plateau-type instability. For higher void-branch density, 3D islands are directly let behind the branches crossover without the help of any Rayleigh-Plateau-type instability.

C. Kinetics and activation energy for dewetting

The dewetted area versus time is reported in Fig. 5. In the early stages of dewetting (when the dewetted area is star shaped), the dewetted area grows linearly with time (red line in Fig. 5). For longer times, multibranches develop

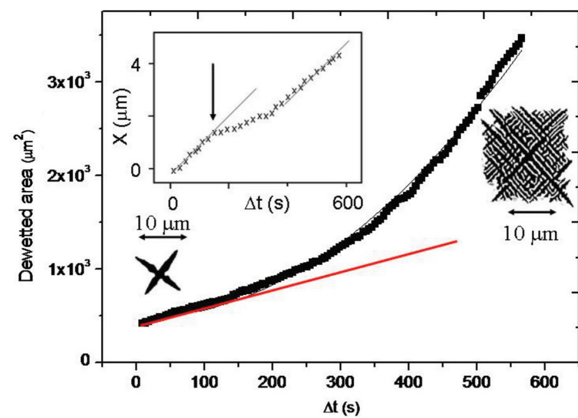

FIG. 5. (Color online) Dewetting area versus time from the star-shaped regime towards the multibranch configuration. The velocity of a typical void tip is given in the inset. The black arrow corresponds to the apparition of a secondary tip. The LEEM images, obtained at the beginning and at the end of the process, are also reported as binary images (the Ge matter in white, the opening void in black).

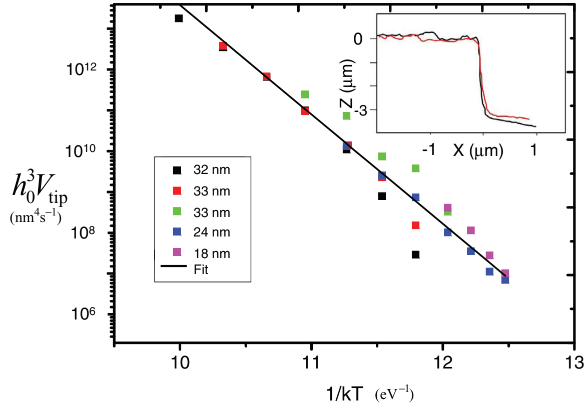

FIG. 6. (Color online) $\ln(h_0^3 V_{tip})$ versus $1/k_B T$ recorded for various thicknesses. The continuous line is the best fit obtained from Eq. (1). Inset: typical tip profiles measured by AFM.

inside a square-shaped envelope, and the dewetting area varies quadratically with time. In this regime, a focus on a typical void-tip velocity is reported in the inset of Fig. 5. It grows linearly with time but temporarily slows down each time that a secondary perpendicular branch nucleates then quickly recovers its initial velocity. Two height profiles, measured by AFM in the direction perpendicular to two typical void tips, are reported in the inset of Fig. 6. It can be seen that the void tips have no rim. In other words, the local thickness of the film simply is the initial film thickness h_0.

Since there is no experimental evidence for the occurrence of a rim at the void tips, we can write the void-tip velocity as[9,11]

$$V_{tip} = \frac{D_0 c}{k_B T} \frac{\Omega^2}{\pi a^2} \frac{2E_s}{h_0^3} e^{-E^{diff}/k_B T}, \tag{1}$$

where $c = c_0 e^{-E^{form}/k_B T}$ is the fraction of diffusing species with E^{form} as the formation energy of the diffusing species, $D_s = D_0 e^{-E^{diff}/k_B T}$ is the surface diffusion constant, E^{diff} is the diffusion energy, and $E_s = \gamma_{Si} + \gamma_{Si/SiO_2} - \gamma_{SiO_2}$ is the surface/interface energy balance, where γ_i is the surface energy of material $i = \mathrm{Si, SiO_2}$ and $\gamma_{i/j}$ is their interfacial energy. The other geometric quantities are Ω, the atomic volume, a, the in-plane atomic distance, and h_0, the local thickness of the film. Equation (1) has been obtained by using the expressions of Refs. 9 and 11, valid for a receding rim of local height h and local width w with $h = h_0$ and $w = \pi h_0/2$ when assuming the tip edge to be a part of a circle. Notice that Eq. (1) has also been written by Jiran and Thompson[29] but with γ_{Si} in place of E_s.

Experimental values of V_{tip} have also been recorded in the stationary regime where the density of branches is high enough to ensure a meaningful measurement of the mean velocity of a significant ensemble of tips. In order to compare samples with different initial Ge thicknesses, in Fig. 6, we have plotted $\ln(h_0^3 V_{tip})$ as a function of $1/k_B T$. Since Eq. (1) is not a simple Arrhenius equation, experimental results have been fitted with $\ln(B/k_B T) - E/k_B T$. This fit is in clear agreement with the experimental data (see Fig. 6). It enables us to extract the activation energy $E = E^{form} + E^{diff} = 2.7 \pm 0.2$ eV as well as the prefactor $\ln(B) = \ln(\frac{2\Omega^2}{\pi a^2} D_0 c_0 E_s) = 42.9 \pm 1.6$.

TABLE II. Literature data: Activation energies for the formation of Ge monomers and Ge dimers. Notice that the formation energy of the Ge monomer (E^{form}_{mo}) has been evaluated by adding the energy necessary to break a dimer 0.33 eV (Ref. 24) to the energy E^{form}_{di} necessary to form a dimer. Thus, it is likely overestimated.

	E^{form} (eV)	E^{diff} (eV)
Monomers	$\sim 1.8 \pm 0.2$	0.37 (Ref. 30)
Dimers	1.5 ± 0.2 (Refs. 31 and 32)	0.86 ± 0.3 (Ref. 33)

The activation energy we found here is in fair agreement with the value of 2.6 ± 0.3 eV found from independent GISAXS measurements of the Ge/$a\mathrm{SiO_2}$ agglomeration kinetics.[16] From literature data (see Table II), the activation value that we find ($E = 2.7 \pm 0.2$ eV) seems compatible with the diffusion of dimers, even if, accounting for the error bars, it is quite difficult to conclude on the nature of the diffusing species. However, a dimer diffusion is surprising since, in the temperature range under study, monomers' activation is expected.[23] Thus, we believe that the diffusion energy we have determined here does not correspond to the simple diffusion on the top (001) surface of the film. Actually, the derived diffusion energy is probably a mean-activation energy corresponding to the diffusion on the whole edge profile, meaning from the triple line towards the Ge(001) surface.

The value of $\ln(B)$ enables us to estimate that 8.6×10^{17} eV s^{-1} $< D_o c_0 E_s < 2.2 \times 10^{19}$ eV s^{-1} when using, for Ge(001), $a = a_0/\sqrt{2}$ with the Ge crystallographic parameter $a_0 = 0.566$ nm. It results in 3×10^5 nm^2 s^{-1} $< DcE_s <$ 7×10^6 nm^2 s^{-1} at 840 °C. This value is in fair agreement with the mean value $DcE_s \approx 4 \times 10^6$ nm^2 s^{-1}, obtained from independent experiments.[16] It is also comparable to the value of 4×10^6 nm^2 s^{-1}, reported for Si by Keeffe *et al.*[34] in the same temperature range. The value of E_s can be estimated from Table III where the data available in literature are reported. For γ_{SiO_2}, we have used the value calculated in Ref. 35 that is in fair agreement with the experimental value estimated from the surface tension of silica of 300 mJ m^{-2}, measured at 1700 °C and corrected from a mean-temperature coefficient of -0.15 mJ m^{-2} K^{-1} given in Ref. 36. For Si and Ge, we have reported experimental values. Within the uncertainties, we can, thus, estimate $E_s \approx 10 \pm 2$ eV nm^{-2}. This value is quite similar to the value calculated for Si(001)/$a\mathrm{SiO_2}$ that is within the range of $E_s \sim$ 7–15 eV nm^{-2}.[9]

TABLE III. Literature data for surface energies (γ_i) and interfacial energies (γ_{i/SiO_2}). These values lead to E_s on the order of 1600 mJ m^{-2} that means $E_s \approx 10 \pm 2$ eV/nm^2 since uncertainties are estimated to 20%.

i	γ_i (mJ m^{-2})	γ_{i/SiO_2} (mJ m^{-2})
Si	1240 (Ref. 37)	1280 (Ref. 38)
Ge	1100 (Ref. 37)	1000 (Ref. 39)
SiO_2	430 (Ref. 35)	

TABLE IV. Synthesis of experimental results. For Si, all the results originate from Refs. 9, 11, and 6.

	Ge at $T = 800\,^{\circ}$C	Ge at $T = 890\,^{\circ}$C	Si at $T = 825\,^{\circ}$C
Main morphology	Cross then sparse dendrites	Cross then dense dendrites	Square voids
Facets seen in GISAXS	{15 3 23}{133}{111}	{133}{111}	{133}{111}
Void-tip shape	Along ⟨100⟩ faceted	Along ⟨100⟩ rounded	Along ⟨110⟩
Nanowires faceting along:	Principal ⟨510⟩, secondary ⟨310⟩	Principal ⟨310⟩, secondary ⟨510⟩	⟨110⟩
Velocity anisotropy	$V_{110} > V_{100}$	$V_{110} > V_{100}$	$V_{110} < V_{100}$
Stable fronts	No stable front	No stable front	⟨110⟩

V. STABILITY AND ANISOTROPY OF DEWETTING: COMPARISON WITH SOI

As mentioned in the Introduction, a comparison with Si(001)/aSiO$_2$ results, described in Refs. 9, 11, and 6, should help to understand the stability conditions and the velocity anisotropy. For this purpose, our main results are summarized in Table IV. Notice that the stability properties of the dewetting fronts reported in the last line of Table IV result from the real-time observation of the dewetting fronts from artificial well-oriented edges obtained by electronic lithography as described in Ref. 6.

Stereographic projections of the facets detected by GISAXS experiments for both Si/aSiO$_2$ and Ge/aSiO$_2$ systems are reported in Fig. 7. The so-observed facets belong to the shaded disk in Fig. 7, whereas, the outer disk contains all the possible facets of the free equilibrium shape. The two circles do not coincide because, due to its adhesion on SiO$_2$, only a part of the free equilibrium shape emerges above the substrate defining an emerging height H.[40] The ratio between both circles is about 0.8. Notice that, for Ge, the aspect ratio measured on 3D islands by AFM is greater at high temperatures (0.75 ± 0.05) than at low temperatures (0.55 ± 0.05). It is consistent with GISAXS data since the {311} facets can only be seen on the most emerging shapes (Fig. 7).

The [110] front is the zone axis of the (113) and (111) facets. These facets stabilize the [110] front which, as a consequence, recedes keeping its straight shape.[6] On the contrary, Si-[100] fronts are destabilized by the presence of (311) and (111) facets and, thus, recede by the formation of Si fingers separated by void fingers faceted with (113) and (111) facets in order to

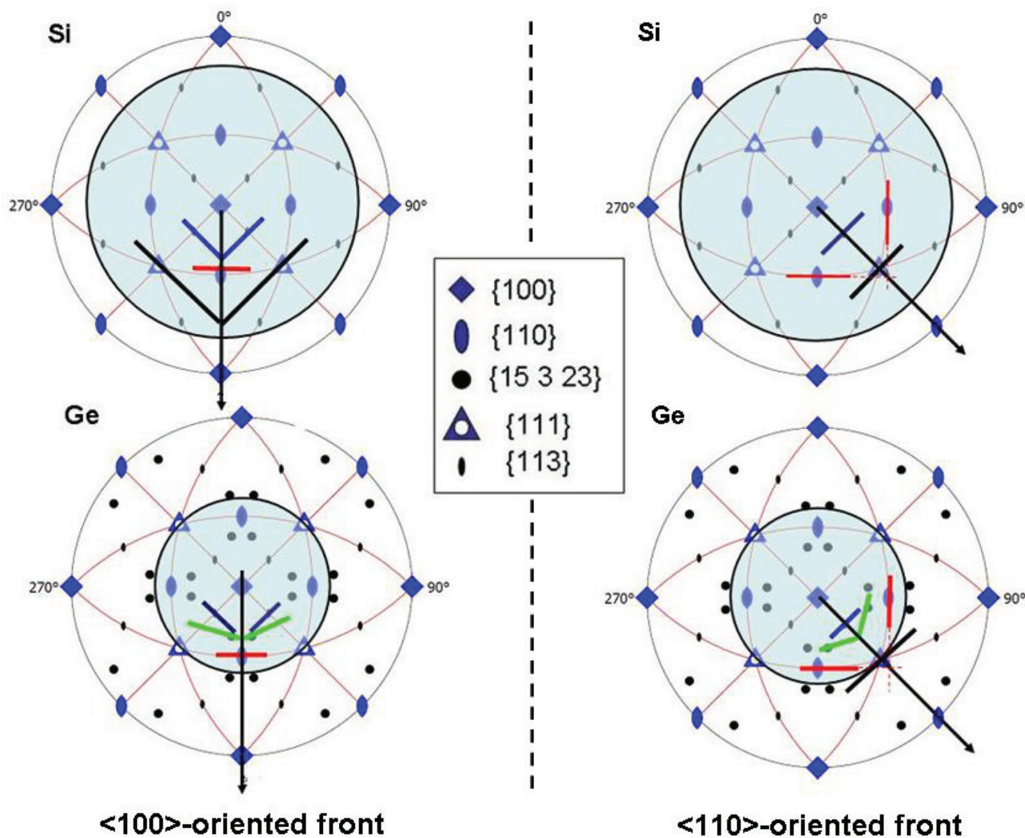

FIG. 7. (Color online) Stereographic projections of the facets detected by GISAXS for Si (top) and for Ge (bottom). The tracks of the facets are schemed in colored bars: black for {111}, red for {110}, blue for {113}, and green for {15 3 23}. The case for the [100]-directed fronts is presented on the left, whereas, the case for the [110]-oriented fronts is presented on the right.

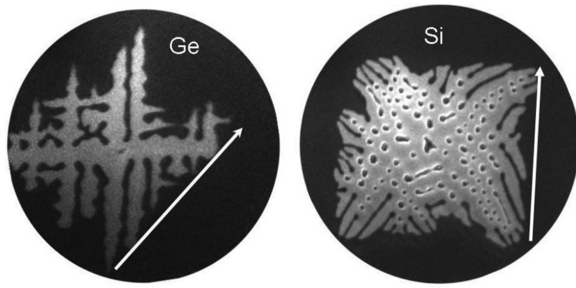

FIG. 8. LEEM images of GOI (field of view 25 μm) and SOI (field of view 25 μm) square voids. The arrow corresponds to the [100] direction for Ge but to the [110] direction for Si.

locally reform [110] stable fronts.[6] Moreover, there is $V_{110}^{\mathrm{Si}} \ll V_{100}^{\mathrm{Si}}$.[6]

For Ge at $T < T_R$, {15 3 23} facets have extended areas, whereas, due to the low Ge emerging height, {111} facet areas are limited. The Ge-[110] fronts and the Ge-[100] fronts are, thus, destabilized by the {15 3 23} facets. Moreover, the orientation of the void branch and the orientation of the edges (Fig. 8) of the dewetted area show that $V_{110}^{\mathrm{Ge}} > V_{100}^{\mathrm{Ge}}$. A consequence of the absence of stable fronts is that Ge void tips do not develop facets contrary to Si void tips. For the same reason, the edges of the nanowires leaved by the crossing of the void branches are parallel to the [110] directions but tend to be destabilized by the {15 3 23} facets giving birth to the ⟨510⟩ orientations [Fig. 4(d)]. However, the ⟨310⟩ directions are not excluded because of the role played by the {311} facets.

For Ge at $T > T_R$, the {15 3 23} facets are no longer present, and the {311} facets are observed [Figs. 1(e) and 1(f)]. The reappearance of the {311} facets, compared to the low-temperature case, likely has a kinetics origin since the island shapes should be closer to their equilibrium shapes at high temperatures than at low temperatures (where surface diffusion is less active). However, we cannot exclude a temperature effect on the equilibrium shape itself.[40,41]

It could be natural to think that the dewetting properties of the Ge(001)/aSiO$_2$ and Si(001)/aSiO$_2$ systems should be similar in the high-temperature regime where both systems exhibit the same facets (Table IV). However, it is not the case since, experimentally, we observe that: (i) the edge orientation of the Ge dewetting zone is rotated by 45° with respect to the Si dewetting zones (see Fig. 8), and (ii) the Ge-⟨110⟩-oriented front is unstable during dewetting, whereas, the Si-⟨110⟩-oriented front is stabilized by the {111} and {113} Si facets and recedes at constant shapes.[6] We believe that this discrepancy originates from the destabilization of the Ge⟨110⟩ front by the {15 3 23} orientation, even if the {15 3 23} facets have disappeared (above the roughening temperature). Indeed, above T_R, the {15 3 23} facets are replaced by rounded parts, that are sufficient to prevent the [110] front from remaining straight. This is also illustrated in the shape of the Ge void tips that are more rounded at 890 °C than at lower temperatures.

Finally, we find, that Dc is of the same order for Si and Ge. It is quite surprising since, at the same temperature, the dewetting velocity is 2 orders of magnitude higher for Ge than for Si![11] The weak point, leading to this apparent paradox, is that the Si

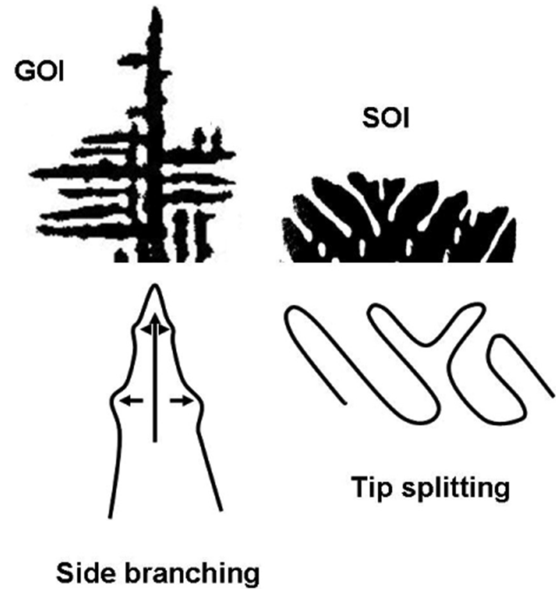

FIG. 9. Top: dewetted morphology; bottom: side-branching and tip-splitting mechanisms.

and Ge dewetting morphologies actually are different. Indeed, as shown in Fig. 9, Ge dewetting proceeds by side-branching mechanisms, whereas, Si dewetting proceeds by tip splitting. More precisely, for Si, the dewetting proceeds by the opening of square voids with an edge destabilization that leads to the collective formation of periodic fingers,[6,11] whereas, for Ge, the dewetting proceeds by the growth of quasi-independent void branches with successive side branching (Fig. 9). As described in Ref. 11, the collective behavior, valid for Si, leads to an effective thickness-dependent activation energy that, for instance, overpasses 3 eV for 20-nm-thick Si films.[11] This is not observed for the Ge/a-SiO$_2$ system. In other words, whereas, the velocity of Ge void tips can really be described by a 1D model where the tips behave independently, it is not the case of Si for which the simultaneous formation of fingers leads to 2D corrections of the expression of the velocity that is equivalent to define an effective activation energy in Eq. (1). Furthermore, the local rim of height $h > h_0$ that exists at the Si void tip also contributes to slowing down the velocity of the Si front.

VI. CONCLUSION

The dewetting properties of Ge(001)/aSiO$_2$ have been studied above and beneath the roughening temperature $T_R \approx 850$ °C of the {15 3 23} facet.

At $T < T_R$, the role of the facets on the dewetting properties has been confirmed. Indeed, for Si(001)/aSiO$_2$, the ⟨110⟩-oriented fronts are stabilized by {113} and {111} facets that have a common ⟨110⟩ zone axis. It is not the case for Ge(001)/aSiO$_2$ where the presence of {15 3 23} facets associated with the small size of the {111} facets is at the origin of the destabilization of the Ge-⟨110⟩ fronts. These {15 3 23} facets limit the dynamics of the Ge front with three remarkable consequences: (i) The Ge fingers are aligned along the ⟨110⟩ direction, which is the bisector of the (15 3 23) and (15 $\bar{3}$ 23) facets, so that the Ge fingers are 45° rotated with respect to the

Si fingers (Figs. 7 and 8), (ii) the {111} and {113} facets that develop along the Ge fingers (their ⟨110⟩ zone axis), increase the fingers' stability so that the island formation is delayed (with respect to Si) stabilizing Ge nanowires, (iii) there is an inversion of the velocity anisotropy for Ge with respect to Si: $V_{110}^{Ge} > V_{100}^{Ge}$, whereas, $V_{110}^{Si} < V_{100}^{Si}$.

At $T > T_R$, the {15 3 23} facets disappear, and the {311} facets re-introduce. However, it is not enough to restabilize the Ge-⟨110⟩ front because the sizes of the {113} and {111} facets are too small and because of the perturbation due to the rounded part originating from the roughening transition of the {15 3 23} facets. For Si(001)/aSiO$_2$, the {113} and {111} facets are sufficient to stabilize the Si-⟨110⟩ front.[6]

Experimental data enable us to extract the activation energy for the Ge dewetting velocity at 2.7 ± 0.2 eV. Finally, the weak energetics differences between Si and Ge are sufficient to change the dewetting morphology from squared-void dewetting for Si to more dendritic-like dewetting for Ge. These morphological differences are at the origin of the difference between the dewetting velocities of Si and Ge despite quite similar diffusivity and driving force values.

ACKNOWLEDGMENTS

This work was supported by an APO grant delivered by the PACA Region Council and by an ANR grant in the framework of the LOTUS project. The authors would like to thank the beamline BM32 staff from help during beam access at the synchrotron facility ESRF in Grenoble. The authors also acknowledge S. Curiotto for fruitful discussions.

*leroy@cinam.univ-mrs.fr
†cheynis@cinam.univ-mrs.fr
‡muller@cinam.univ-mrs.fr

[1] D. J. Srolovitz and S. A. Safran, J. Appl. Phys. **60**, 247 (1986).
[2] D. J. Srolovitz and S. A. Safran, J. Appl. Phys. **60**, 255 (1986).
[3] F. Cheynis, F. Leroy, and P. Müller, C. R. Phys. (to be published).
[4] H. Wong, P. Voorhees, M. Miksis, and S. Davis, Acta Mater. **48**, 1719 (2000).
[5] E. Dornel, J.-C. Barbé, F. de Crécy, G. Lacolle, and J. Eymery, Phys. Rev. B **73**, 115427 (2006).
[6] F. Leroy, F. Cheynis, T. Passanante, and P. Müller, Phys. Rev. B **85**, 195414 (2012).
[7] J. Ye and C. Thompson, Acta Mater. **59**, 582 (2011).
[8] M. Dufay and O. Pierre-Louis, Phys. Rev. Lett. **106**, 105506 (2011).
[9] E. Bussmann, F. Cheynis, F. Leroy, P. Müller, and O. Pierre-Louis, New J. Phys. **13**, 043017 (2011).
[10] D. T. Danielson, D. Sparacin, J. Michel, and L. Kimerling, J. Appl. Phys. **100**, 083507 (2006).
[11] F. Cheynis, E. Bussmann, F. Leroy, T. Passanante, and P. Müller, Phys. Rev. B **84**, 245439 (2011).
[12] J. Margrave, *The Characteristics of High Temperature Vapors* (Wiley, New York, 1967).
[13] B. Ghyselen, J. Hartmann, T. Ernst, C. Aulnette, B. Osternaud, Y. Bogumilowicz, A. Abbadie, P. Besson, O. Rayssac, A. Tiberj, N. Daval, I. Cayrefourq, F. Fournel, H. Moriceau, C. Dinardo, F. Andrieu, V. Paillard, M. Cabie, L. Vincent, E. Snoeck, F. Cristiano, A. Rocher, A. Ponchet, A. Claverie, P. Boucaud, M. Semeria, D. Bensahel, N. Kervenez, and C. Mazure, Solid-State Electron. **48**, 1285 (2004).
[14] E. Augendre, L. Sanchez, L. Benaissa, T. Signamarcheix, J. Hartmann, C. L. Royer, M. Viner, W. V. den Daele, J. Damlencourt, K. Romanjek, A. Poydebasque, P. Batude, C. Tabone, F. Mazen, A. Tauzin, N. Blanc, M. Pellat, J. Dechamp, M. Zussy, P. Scheiblin, M. Jaud, C. Drazek, C. Maurois, M. Piccin, A. Abbadie, F. Lallement, N. Daval, E. Guiot, A. Rigny, G. Ghyselen, K. Bourdelle, F. Boulanger, S. Cristoloveanu, T. Billon, O. Faynot, C. Degeut, and L. Clavelier, ECS Trans. **25**, 351 (2009).
[15] E. Bussmann, F. Cheynis, F. Leroy, and P. Müller, IOP Conf. Ser.: Mater. Sci. Eng. **12**, 012016 (2010).
[16] F. Cheynis, F. Leroy, T. Passanante, and P. Müller, Appl. Phys. Lett. **102**, 161603 (2013).
[17] G. Renaud, R. Lazzari, and F. Leroy, Surf. Sci. Rep. **64**, 255 (2009).
[18] Z. Gai, X. Li, R. G. Zhao, and W. S. Yang, Phys. Rev. B **57**, R15060 (1998).
[19] Z. Gai, R. G. Zhao, X. Li, and W. S. Yang, Phys. Rev. B **58**, 4572 (1998).
[20] Z. Gai, W. S. Yang, R. G. Zhao, and T. Sakurai, Phys. Rev. B **59**, 15230 (1999).
[21] F. Ross, R. Tromp, and M. Reuter, Science **286**, 1931 (1999).
[22] A. Stekolnikov and F. Bechstedt, Phys. Rev. B **72**, 125326 (2005).
[23] E. van Vroonhoven, H. J. W. Zandvliet, and B. Poelsema, Phys. Rev. Lett. **91**, 116102 (2003).
[24] A. D. Johnson, C. Norris, J. W. M. Frenken, H. S. Derbyshire, J. E. MacDonald, R. G. Van Silfhout, and J. F. Van Der Veen, Phys. Rev. B **44**, 1134 (1991).
[25] W. Kan and H. Wong, J. Appl. Phys. **97**, 43515 (2005).
[26] J. S. Langer, Phys. Rev. A **36**, 3350 (1987).
[27] R. Pieters and J. Langer, Phys. Rev. Lett. **56**, 1948 (1986).
[28] O. Shochet, K. Kassner, E. Ben-Jacob, S. Lipson, and H. Muller-Krumbhaar, Physica A **187**, 37 (1992).
[29] E. Jiran and C. V. Thompson, J. Electron. Mater. **19**, 1153 (1990).
[30] L. Huang, F. Liu, and X. G. Gong, Phys. Rev. B **70**, 155320 (2004).
[31] P. Kruger and J. Pollmann, Phys. Rev. Lett. **74**, 1155 (1995).
[32] E. van Vroonhoven, H. Zandvliet, and B. Poelsema, Surf. Sci. Lett. **574**, L23 (2005).
[33] T. Afanasievia, S. Bulavenko, I. Koval, and H. Zandvielt, J. Appl. Phys. Lett. **93**, 1452 (2003).
[34] M. E. Keeffe, C. Umbach, and J. Blakely, J. Phys. Chem. Solids **55**, 965 (1994).
[35] C. Chuang, Q. Li, D. Leonhardt, S. Han, and T. Sinno, Surf. Sci. **609**, 221 (2013).
[36] K. Mills and B. Keene, Int. Mater. Rev. **32**, 1 (1987).
[37] R. Kern, G. LeLay, and J. J. Métois, in *Current Topics in Materials Science*, edited by E. Kaldis (North-Holland, Amsterdam, 1979), Vol. 3, p. 135.
[38] L. T. Kong and L. J. Lewis, Phys. Rev. B **77**, 085204 (2008).
[39] J. Du and P. Kroll, J. Non-Cryst. Solids **356**, 2448 (2010).
[40] P. Müller and R. Kern, Surf. Sci. **457**, 229 (2000).
[41] P. Müller and R. Kern, Appl. Surf. Sci. **164**, 68 (2000).